CFD Simulations of Turbulent Fluid Flow and Dust Dispersion in the 20 Liter Explosion Vessel

A. Di Benedetto
Dipartimento di Ingegneria Chimica, dei Materiali e della Produzione Industriale, Università degli Studi di Napoli Federico II, Piazzale Tecchio 80, 80125, Napoli, Italy

P. Russo
Dipartimento di Ingegneria Chimica Materiali Ambiente, Università di Roma "La Sapienza", via Eudossiana 18, 00184, Roma, Italy

R. Sanchirico and V. Di Sarli
Istituto di Ricerche sulla Combustione - Consiglio Nazionale delle Ricerche (IRC—CNR), Piazzale Tecchio 80, 80125, Napoli, Italy

DOI 10.1002/aic.14029
Published online March 6, 2013 in Wiley Online Library (wileyonlinelibrary.com)

A CFD model was developed with the aim at simulating the turbulent flow field induced by dust feeding and dispersion within the 20 L bomb, and the associated effects on the distribution of dust concentration. The model was validated considering a set of data (pressure time histories and root mean square velocity) available in the literature. The time sequences of velocity vector and kinetic energy maps have shown that multiple turbulent vortex structures are established within the sphere. These vortices generate dead volumes for the dust which is pushed toward the walls of the sphere. The obtained results are relevant to the practice of dust explosion testing and the interpretation of test results and, then, they should be taken as reference to improve the conditions for standard tests. © 2013 American Institute of Chemical Engineers *AIChE J*, 59: 2485–2496, 2013
Keywords: process safety, dust explosion, cfd simulations, 20 L bomb, turbulence, dust dispersion

Introduction

In chemical processes (food, pharmaceutical and wood industries, chemical manufacturing), a high number of accidents are imputable to explosions of flammable dusts causing failure to equipment, injuries and damages to people and surrounding environment. According to the CSB Investigation Report,[1] from 1980 to 2005, 281 major combustible dust accidents occurred, killing 119 workers, injuring 718 others, and destroying many of the industrial facilities. Recently, a huge explosion occurred in a textile industry located in Biella (Italy)[2] involving flocks coming from wool processing.

Furthermore, in recent years, because of the possibilities concerned with the formation of hybrid mixtures (i.e., mixtures of flammable gas/vapor and dusts) at industrial scale, attention has also been paid toward the basic understanding of such systems.[3–7]

Prevention and mitigation measures are based on the knowledge of the main parameters which characterize the flammability (minimum ignition energy, MIE; minimum ignition temperature, MIT; minimum explosible concentration, MEC; limiting oxygen concentration, LOC), and explosion (maximum explosion pressure, $P_{MAX;}$ deflagration index, K_{st}) features of dust-air and/or dust/gas-air mixtures. Both experimental[8] and theoretical/numerical[9–11] explosion tests may be performed for the evaluation of these parameters.

Experimental tests are performed according to the American Society for Testing and Materials (ASTM) Method E 1226 (2003), the National Fire Protection Association (NFPA) Standard 68 (1994), the German Society of Engineers (VDI) Method 3673 (1995), and the International Standards Organization (ISO) Method 6184/1.[12]

According to these procedures, explosion tests are performed in a spherical vessel (the 20 L sphere or the 1 m^3 sphere). In the ASTM E 1226 protocol (ASTM, 2003), the dust-air cloud is obtained by injecting the dust in the sphere, initially pre-evacuated at 0.4 bar, through a valve connecting a container loaded with dust and pressurized with 21 bar of compressed air. At the bottom side of the bomb, a rebound nozzle is placed to allow dispersion of the dust-air mixture inside the vessel.

The main issues of this procedure are the preignition turbulence level and the dust dispersion, mixing and homogeneity. The preignition turbulence plays a major role in affecting the explosion behavior (flame propagation velocity, pressure time history and deflagration index).[13,14] As a result, the control of the turbulence level is of primary importance. Also, the homogeneous dispersion of the dust-air mixture in the vessel significantly affects the flame propagation, if stratification and sedimentation occur.

Correspondence concerning this article should be addressed to A. Di Benedetto at almerinda.dibenedetto@unina.it.

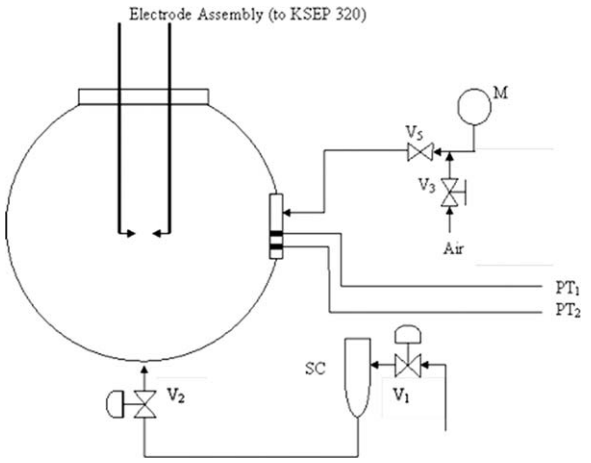

Figure 1. 20 L bomb for the determination of dust explosion parameters.

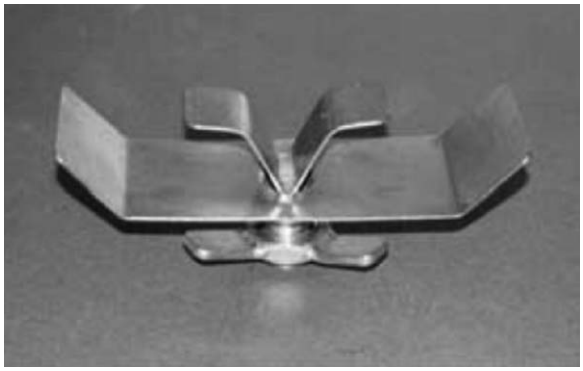

Figure 2. Rebound nozzle.

Dust injection inside the vessel produces a turbulent fluid flow which decays over time. The timing between the turbulence decay and the mixture ignition is of major relevance, since the flame propagation is significantly affected by the preignition turbulence level.[13] Bartknecht[15] and Siwek[16] compared results of explosion tests carried out both in the 20 L and the 1 m^3 spheres. They found similar results when using an ignition delay time after injection equal to 60 ms for the 20 L sphere and equal to 600 ms for the 1 m^3 sphere. This suggests that the same initial turbulence level is attained at different delay times when using the two spheres.

In the past, different authors measured the turbulence level inside three different equipment: the 20 L sphere[17–19]; the 1 m^3 ISO vessel[20] and a 1 m^3 cylindrical vessel.[21] Turbulence measurements were performed by means of hot wire anemometry[17,18,21] or laser doppler anemometry.[19,20] Collected data allowed the evaluation of the temporal values of the instantaneous velocity and of the root mean square velocity fluctuations in few points of the vessel, mainly positioned at the center. Furthermore, the dust cloud formed in these vessels was assumed to be fairly uniform, but this was not demonstrated quantitatively. As a result, the nominal dust concentration (mass of sample/volume of vessel) in the sphere was taken as the representative dust concentration at the time of ignition in the whole sphere. The uniformity of the dust concentration in the sphere is of primary importance not only for measurements of K_{st}, but mainly for measurements of MEC.

Recently, Kalejaiye et al.[22] used optical dust probes to measure optical transmittance through the dust cloud at six locations within the 20 L sphere, with the two standard dispersion nozzles (rebound and perforated annular nozzles). They tested dispersion of three dusts (Pittsburgh coal, Gilsonite, and purple K) with different diameters and different concentrations, showing that the transmission data of the three dusts were significantly lower than those corresponding to the nominal value. They attributed this difference in part to the reduction in particle size that occurred during dispersion. These results are, however, qualitative since, from the measured transmission data, it is not possible to derive the corresponding values of the dust concentration.

From all these experimental analyses, complete maps of velocity, turbulence level and dust concentration cannot be derived. Also, from the theoretical side, at the moment no

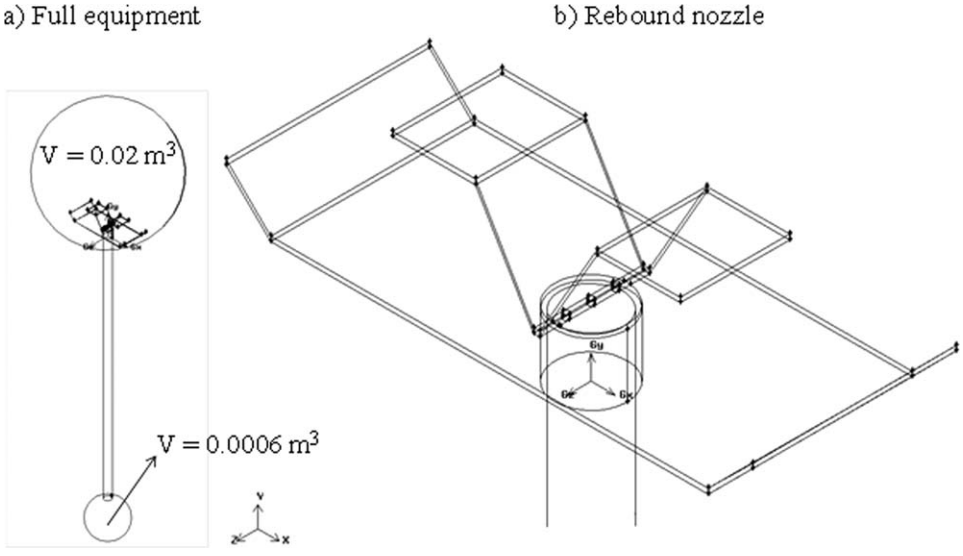

Figure 3. Computational domain: full equipment (a) and detail of the rebound nozzle (b).

Table 1. Geometrical Details of the Computational Domain

Container diameter	0.052 m
Tube diameter	0.02 m
Tube length	0.72 m
Sphere diameter	0.336 m

simulation is available which allows quantification of these maps.

Furthermore, it is not clarified in the literature if the dust particle and the dust concentration play an effective role in the development of the turbulent fluid flow. Accordingly, the standard conditions for explosion tests are the same, whatever the dust size and concentration.

The aim of this work is to gain insights into the fluid flow which is established inside the sphere under the conditions of the standard tests, and to visualize the dust dispersion process. To this end, we developed a CFD model able to simulate the temporal evolution of the fluid flow and the turbulence decay in the 20 L sphere, when injecting either only air or dust-air mixtures.

The Model

The explosion apparatus: 20 l bomb

CFD simulations were run of the standard 20 L sphere apparatus manufactured by Adolf Kühner AG (CH).[16]

The core of the test facility is the spherical explosion chamber. The vessel is made of stainless steel and is rated to resist up to 30 bar (static pressure). The rebound nozzle is connected to the outlet valve V2 (Figure 1). A water jacket surrounds the spherical bomb for the control of the internal wall temperature. For the formation of the dust cloud, a rebound nozzle (Figure 2) is placed at the bottom side of the bomb. This valve is opened and closed pneumatically by means of an auxiliary piston. The input section of the outlet valve is connected to the sample container ($V = 0.0006$ m^3) by means of which the dust is injected into the sphere. The container loaded with dust is pressurized with 21 bar of compressed air. The sphere is also connected (righthand side of Figure 1) to a vacuum line that is used to prepare the dust-air mixture and to provide an initial test pressure equal to 1 bar. The vacuum outlet is connected to a vacuum pump (Vacuubrand RZ9) providing 0.4 bar pressure.

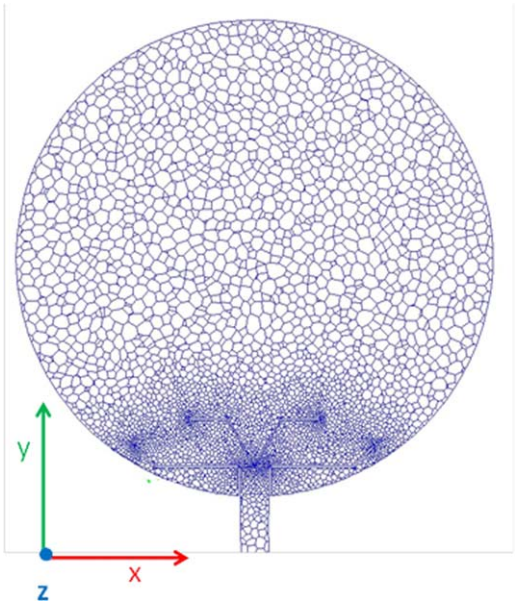

Figure 4. Unstructured and nonuniform mesh used.

[Color figure can be viewed in the online issue, which is available at wileyonlinelibrary.com]

Table 2. Details of the Mesh

20 l Sphere cell number	999435
0.6 l Sphere cell number	17516
Total cell number	1016951

Computational domain and mesh

The computational domain and mesh were built by means of the software Gambit 2.3.16.[23] The sphere was modeled as tridimensional and details of the rebound nozzle were also reproduced. In addition, the container with the feeding tube of the dust was included in the computational domain (Figure 3). In the rebound nozzle, three holes are present which allow the dust-air mixture coming from the sample container to be fed.

In Table 1, geometrical details of the computational domain are given. In Figure 4, the unstructured and nonuniform mesh used is shown, and in Table 2 details of the mesh are given.

Equations

The dust concentration investigated was equal to 250 g/m^3 with a dust density of 2100 kg/m^3, corresponding to a solid fraction equal to $\alpha_p = 1.2\ 10^{-4}$. At these conditions, it was possible to assume the *particle-laden flow* approach in which the Eulerian approach is used for the fluid phase and the Lagrangian approach is used for the solid phase.

The fluid flow was simulated by solving the time-averaged Navier-Stokes equations (Eulerian approach) written in polar coordinates that read as follows (conventional notation was used):

Continuity equation

$$\frac{1}{r^2}\frac{\partial(\bar{\rho}r^2\bar{v}r)}{\partial r}+\frac{1}{r\sin\theta}\frac{\partial(\bar{\rho}\bar{v}_\theta\sin\theta)}{\partial\theta}+\frac{1}{r\sin\theta}\frac{\partial(\bar{\rho}\bar{v}_\phi)}{\partial\phi}=0 \qquad (1)$$

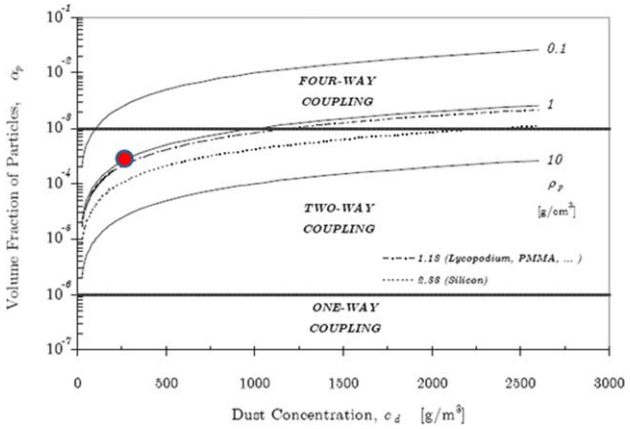

Figure 5. Classification of the interaction between fluid and particles.[25]

[Color figure can be viewed in the online issue, which is available at wileyonlinelibrary.com]

Momentum balance equation, r co-ordinate

$$\bar{\rho}\left(\frac{\partial \bar{v}_r}{\partial t}+\bar{v}_r\frac{\partial \bar{v}_r}{\partial r}+\frac{\bar{v}_\theta}{r}\frac{\partial \bar{v}_r}{\partial \theta}+\frac{\bar{v}_\phi}{r\sin\theta}\frac{\partial \bar{v}_r}{\partial \phi}-\frac{\bar{v}_\theta^2+\bar{v}_\phi^2}{r}\right)=-\frac{\partial p}{\partial r}-\left[\frac{1}{r^2}\frac{\partial}{\partial r}\left(r^2\bar{\tau}_{rr}^{(v)}\right)+\frac{1}{r\sin\theta}\frac{\partial}{\partial \theta}\left(\bar{\tau}_{\theta r}^{(v)}\sin\theta\right)+\frac{1}{r\sin\theta}\frac{\partial}{\partial \phi}\left(\bar{\tau}_{\phi r}^{(v)}\right)-\frac{\bar{\tau}_{\theta\theta}^{(v)}+\bar{\tau}_{\phi\phi}^{(v)}}{r}\right]$$
$$-\left[\frac{1}{r^2}\frac{\partial}{\partial r}\left(r^2\bar{\tau}_{rr}^{(t)}\right)+\frac{1}{r\sin\theta}\frac{\partial}{\partial \theta}\left(\sin\theta\bar{\tau}_{\theta r}^{(t)}\right)+\frac{1}{r\sin\theta}\frac{\partial}{\partial \phi}\left(\bar{\tau}_{\phi r}^{(t)}\right)-\frac{\bar{\tau}_{\theta\theta}^{(t)}+\bar{\tau}_{\phi\phi}^{(t)}}{r}\right]+\bar{\rho}g_r \tag{2}$$

Momentum balance equation, θ co-ordinate

$$\bar{\rho}\left(\frac{\partial \bar{v}_\theta}{\partial t}+\bar{v}_r\frac{\partial \bar{v}_\theta}{\partial r}+\frac{\bar{v}_\theta}{r}\frac{\partial \bar{v}_\theta}{\partial \theta}+\frac{\bar{v}_\phi}{r\sin\theta}\frac{\partial \bar{v}_\theta}{\partial \phi}+\frac{\bar{v}_r\bar{v}_\theta-\bar{v}_\phi^2 cot\theta}{r}\right)=$$
$$-\frac{1}{r}\frac{\partial p}{\partial \theta}-\left[\frac{1}{r^3}\frac{\partial}{\partial r}\left(r^3\bar{\tau}_{r^\theta}^{(v)}\right)+\frac{1}{r\sin\theta}\frac{\partial}{\partial \theta}\left(\bar{\tau}_{\theta\theta}^{(v)}\sin\theta\right)+\frac{1}{r\sin\theta}\frac{\partial}{\partial \phi}\left(\bar{\tau}_{\phi\theta}^{(v)}\right)+\frac{\bar{\tau}_{\theta r}^{(v)}-\bar{\tau}_{r\theta}^{(v)}-\bar{\tau}_{\phi\phi}^{(v)}cot\theta}{r}\right]- \tag{3}$$
$$\left[\frac{1}{r^3}\frac{\partial}{\partial r}\left(r^3\bar{\tau}_{r\theta}^{(t)}\right)+\frac{1}{r\sin\theta}\frac{\partial}{\partial \theta}\left(\bar{\tau}_{\theta\theta}^{(t)}\sin\theta\right)+\frac{1}{r\sin\theta}\frac{\partial}{\partial \phi}\left(\bar{\tau}_{\phi\theta}^{(t)}\right)+\frac{\bar{\tau}_{\theta r}^{(t)}-\bar{\tau}_{r\theta}^{(t)}-\bar{\tau}_{\phi\phi}^{(t)}cot\theta}{r}\right]+\rho g_\theta$$

Momentum balance equation, φ co-ordinate

$$\rho\left(\frac{\partial \bar{v}_\phi}{\partial t}+\bar{v}_r\frac{\partial \bar{v}_\phi}{\partial r}+\frac{\bar{v}_\theta}{r}\frac{\partial \bar{v}_\phi}{\partial \theta}+\frac{\bar{v}_\phi}{r\sin\theta}\frac{\partial \bar{v}_\phi}{\partial \phi}+\frac{\bar{v}_\phi\bar{v}_r-\bar{v}_\theta\bar{v}_\phi\cot\theta}{r}\right)=-\frac{1}{\sin\theta}\frac{\partial p}{\partial \phi}-\left[\frac{1}{r^3}\frac{\partial}{\partial r}\left(r^3\bar{\tau}_{r\phi}^{(v)}\right)+\frac{1}{r\sin\theta}\frac{\partial}{\partial \phi}\left(\bar{\tau}_{\phi\phi}^{(v)}\right)+\frac{\bar{\tau}_{\phi r}^{(v)}-\bar{\tau}_{r\phi}^{(v)}-\bar{\tau}_{\phi\theta}^{(v)}\cot\theta}{r}\right]$$
$$-\left[\frac{1}{r^3}\frac{\partial}{\partial r}\left(r^3\bar{\tau}_{r\phi}^{(t)}\right)+\frac{1}{r\sin\theta}\frac{\partial}{\partial \theta}\left(\bar{\tau}_{\theta\phi}^{(t)}\sin\theta\right)+\frac{1}{r\sin\theta}\frac{\partial}{\partial \phi}\left(\bar{\tau}_{\phi\phi}^{(t)}\right)+\frac{\bar{\tau}_{\phi r}^{(t)}-\bar{\tau}_{r\phi}^{(t)}-\bar{\tau}_{\phi\theta}^{(t)}cot\theta}{r}\right]+\rho g\phi \tag{4}$$

Equations 1–4 were solved by using the standard k-ε model[24] as turbulent submodel.

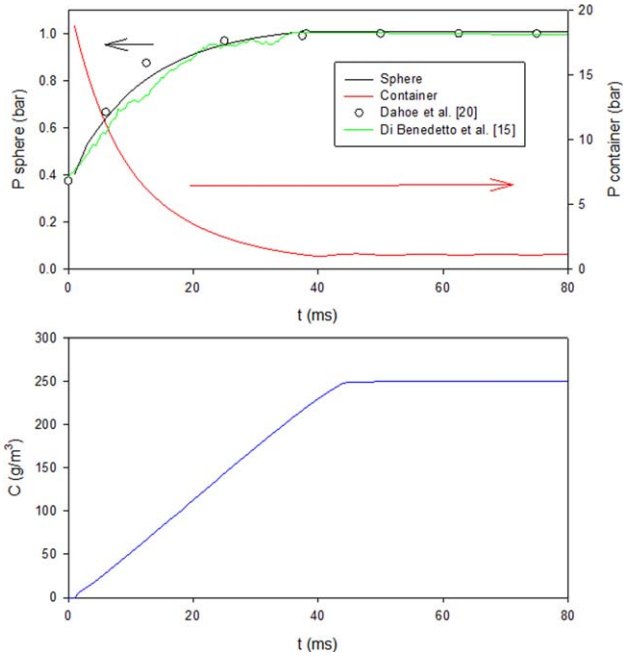

Figure 6. Pressure time histories computed in the sphere and in the container (top); dust concentration in the sphere versus time (bottom) (10 μm dust size and 250 g/m^3 nominal dust concentration).

[Color figure can be viewed in the online issue, which is available at wileyonlinelibrary.com]

The flow of the solid phase was solved using the discrete phase model (DPM) (Lagrangian approach). The interaction between the fluid phase and the solid particles may be of different nature and more specifically one-way, two-way and four-way, depending on the particle volume fraction, particle density and particle concentration.[25]

In Figure 5, the classification proposed by Elghobashi[25] is shown. It appears that, in our conditions (•, particle volume fraction, $\alpha_p = 1.2\ 10^{-4}$; particle density, $\rho_p = 2100$ kg/m^3; particle concentration, C = 250 g/m^3), the nature of the interaction between the fluid phase and the particles is two-way, suggesting that the fluid flow affects the particle motion and vice versa, while the particle–particle collisions (which are accounted for in the four-way coupling) may be neglected.

This assumption is also in agreement with the recent findings by Vreman et al.[26] who showed that, for particle volume fractions larger than 1.5%, the particle–particle interactions play an important role in the development of the flow. The computationally more accessible two-way coupling model proved to give predictions which, for slowly responsive particles and this particle volume fraction, lack a turbophoresis effect and show in the simulations of a vertical gas–solid channel flow the occurrence of a fairly strong "center-jet" which was not recorded in experimental studies.

Table 3. Dust Properties

Dust data	
Density (kg/m^3)	2046
Diameter (μm)	10
Dust concentration (g/m^3)	250

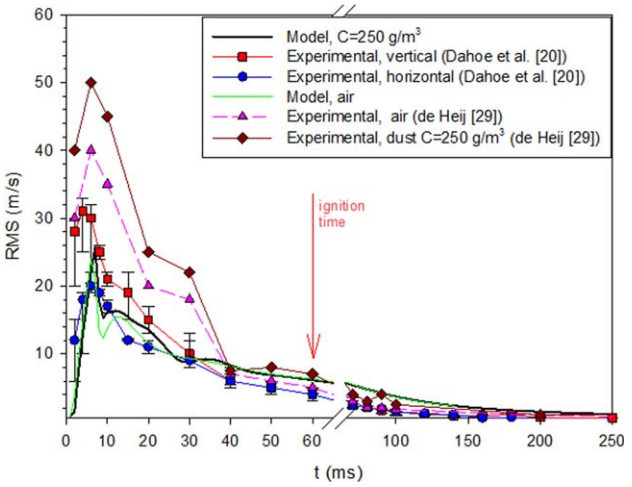

Figure 7. Temporal trend of the root mean square velocity computed when feeding only air (green curve) and a dust-air mixture with 10 μm dust size and 250 g/m^3 dust concentration (black curve).

The experimental data measured by Dahoe et al.[19] and de Heij[28] are also shown. [Color figure can be viewed in the online issue, which is available at wileyonlinelibrary.com]

Furthermore, Lain et al.[27] studied the effect of two-way and four-way coupling approaches in the simulations of flow in pneumatic conveying of solid particles in a horizontal circular pipe. They used two different particle diameters: 200 μm and 50 μm, with a density of 1020 kg/m^3. The main conclusion is that the dynamics of the larger particles (200 μm), being quite inertial, is mainly governed by particle-wall and interparticle collisions, whereas in the case of smaller particles (50 μm) the turbulent fluid-particle interaction plays a significant role. However, from these data, the particle volume fraction cannot be evaluated.

The momentum balance equation of the DPM reads as follows:

$$\frac{du_p}{dt} = F_D(v-u_p) + \frac{g(\rho_p-\rho)}{\rho_p} + F \tag{5}$$

where F is the gravitational force v and ρ are the velocity and density of the fluid phase, while u_p and ρ_p are the velocity and density of the particles.

$F_D(v\text{-}u_P)$ is the drag force per unit mass of particle. F_D is the interphase momentum transfer coefficient and is a function of the Re number according to the following equation

$$F_D = \frac{18\mu}{\rho_P d_p^2}\frac{C_D \mathrm{Re}}{24} \tag{6}$$

where μ is the fluid viscosity and d_p is the diameter of the particles. The Re number in Eq. (6) is a function of the difference between the fluid and the particle velocity

$$Re = \frac{\rho d_p |u_p - v|}{\mu} \tag{7}$$

For the fluid velocity (v) used in Eq. 5, values are not instantaneous, but rather they are constant over a certain time range. The time range is computed as a function of the characteristic time τ_e

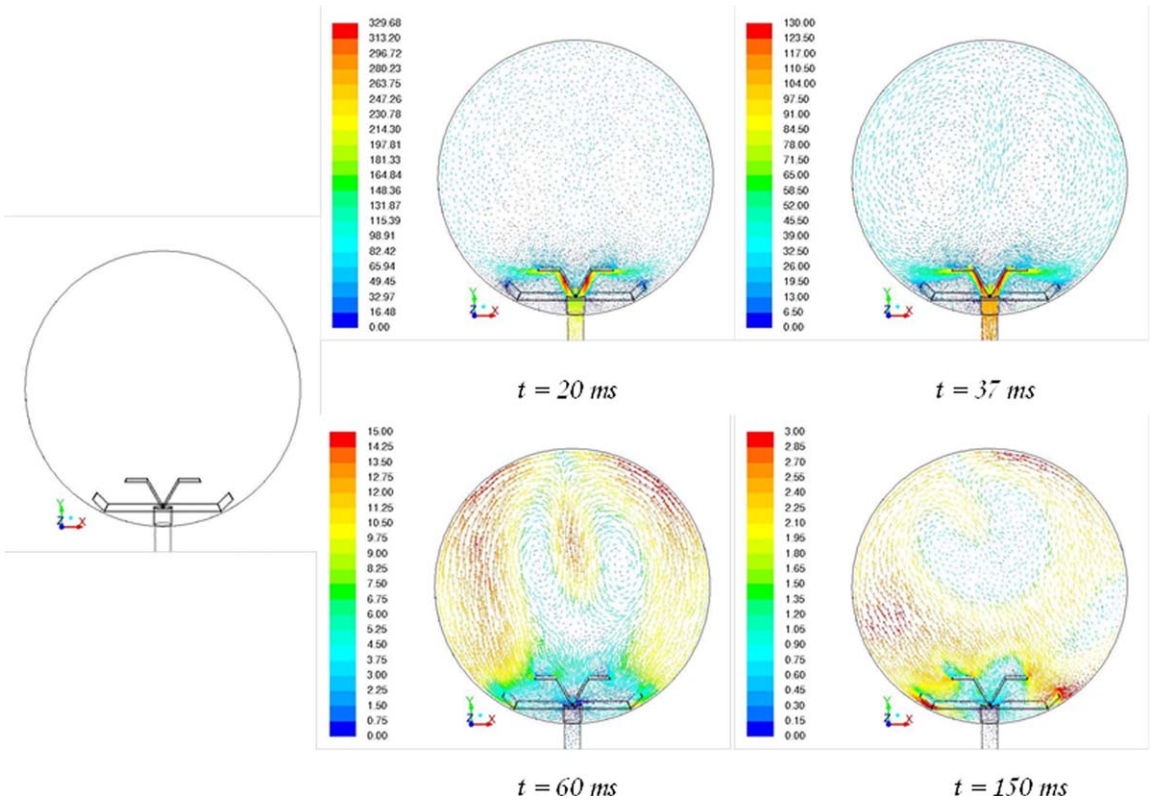

Figure 8. Time sequence of the maps of velocity vectors colored by the velocity magnitude (m/s): frontal view, dust free air.

[Color figure can be viewed in the online issue, which is available at wileyonlinelibrary.com]

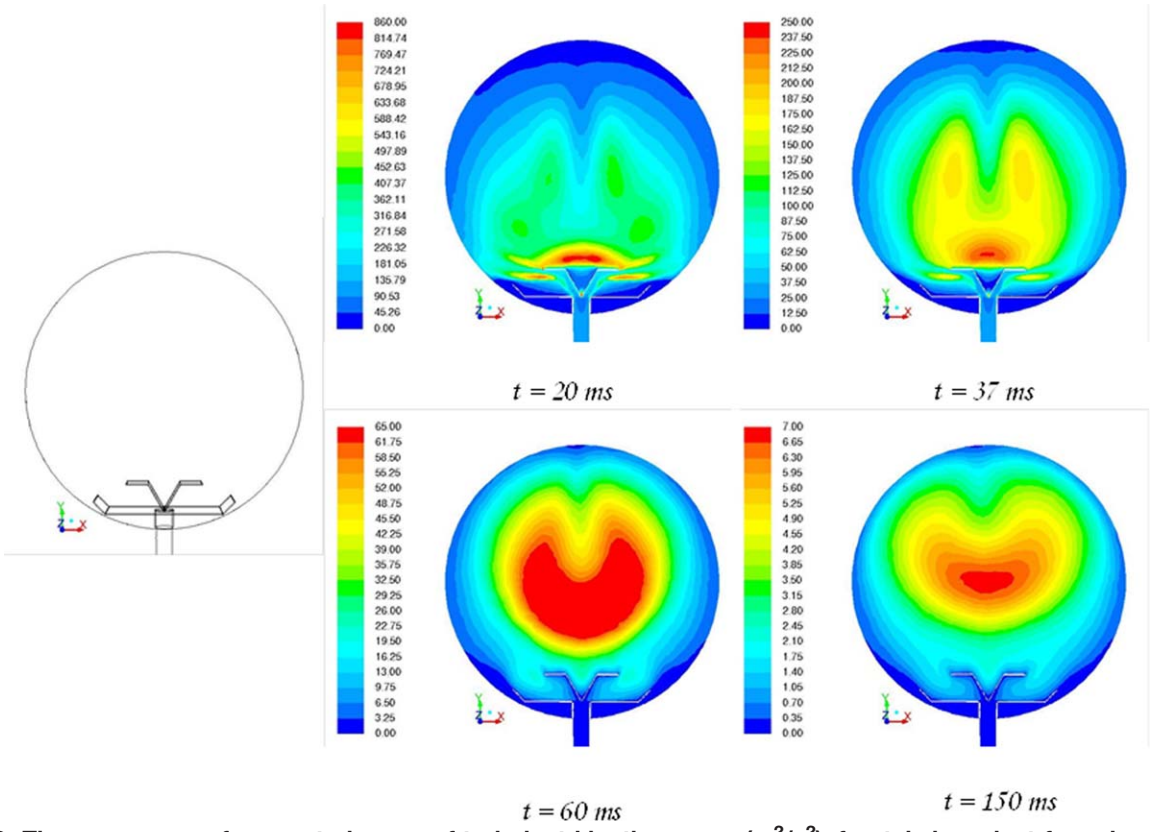

Figure 9. Time sequence of computed maps of turbulent kinetic energy (m^2/s^2): frontal view, dust free air.

[Color figure can be viewed in the online issue, which is available at wileyonlinelibrary.com]

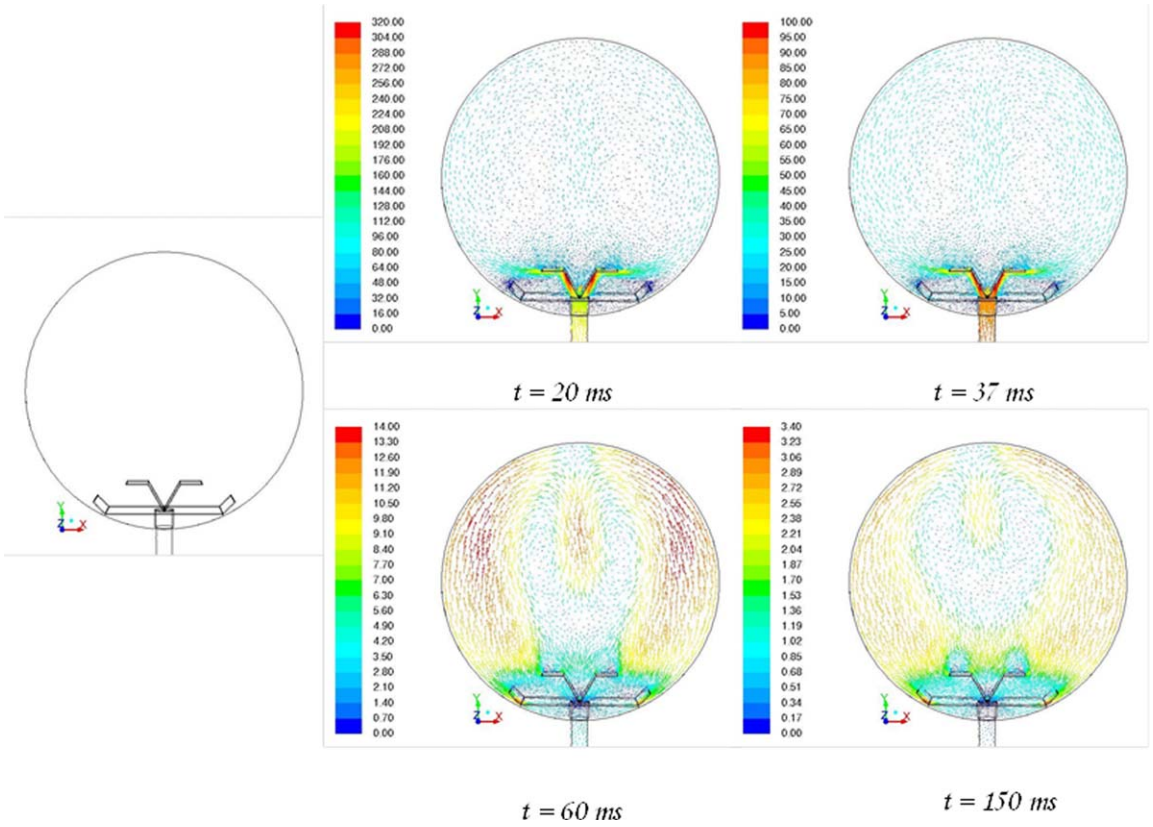

Figure 10. Time sequence of the maps of velocity vectors colored by the velocity magnitude (m/s): frontal view, dust-air mixture.

[Color figure can be viewed in the online issue, which is available at wileyonlinelibrary.com]

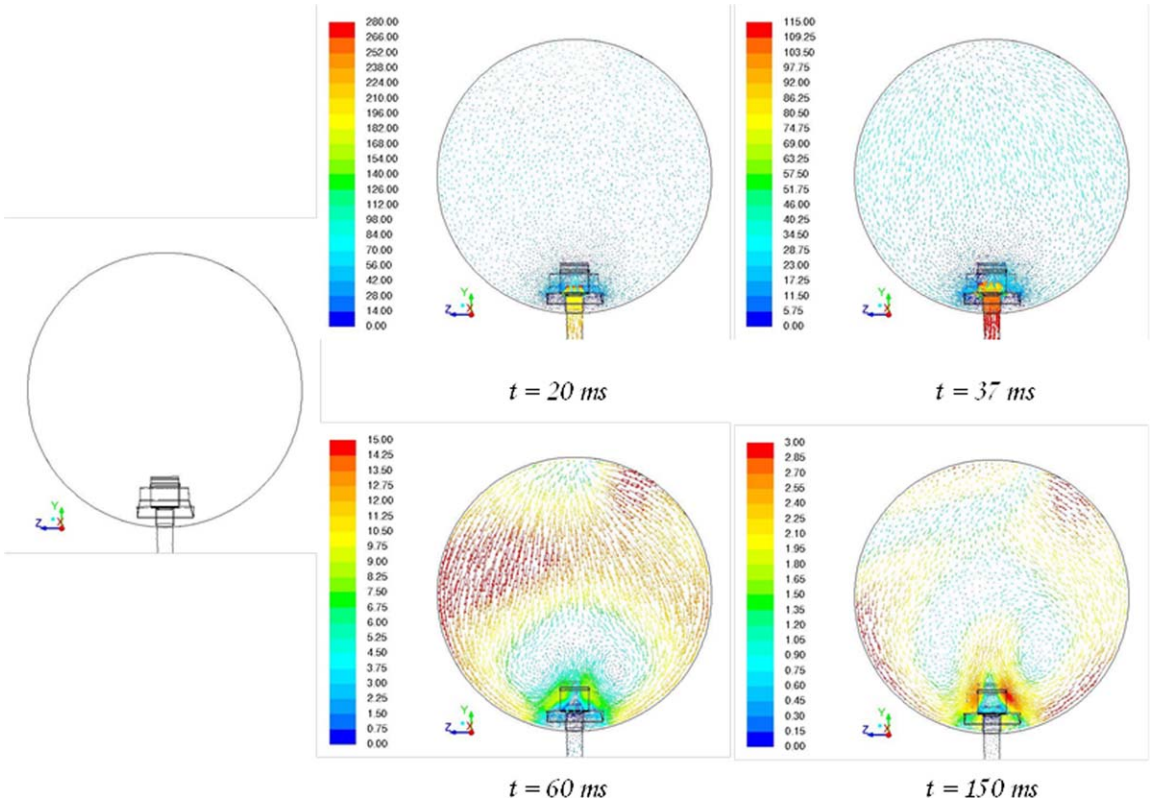

Figure 11. Time sequence of the maps of velocity vectors colored by the velocity magnitude (m/s): lateral view, dust-air mixture.

[Color figure can be viewed in the online issue, which is available at wileyonlinelibrary.com]

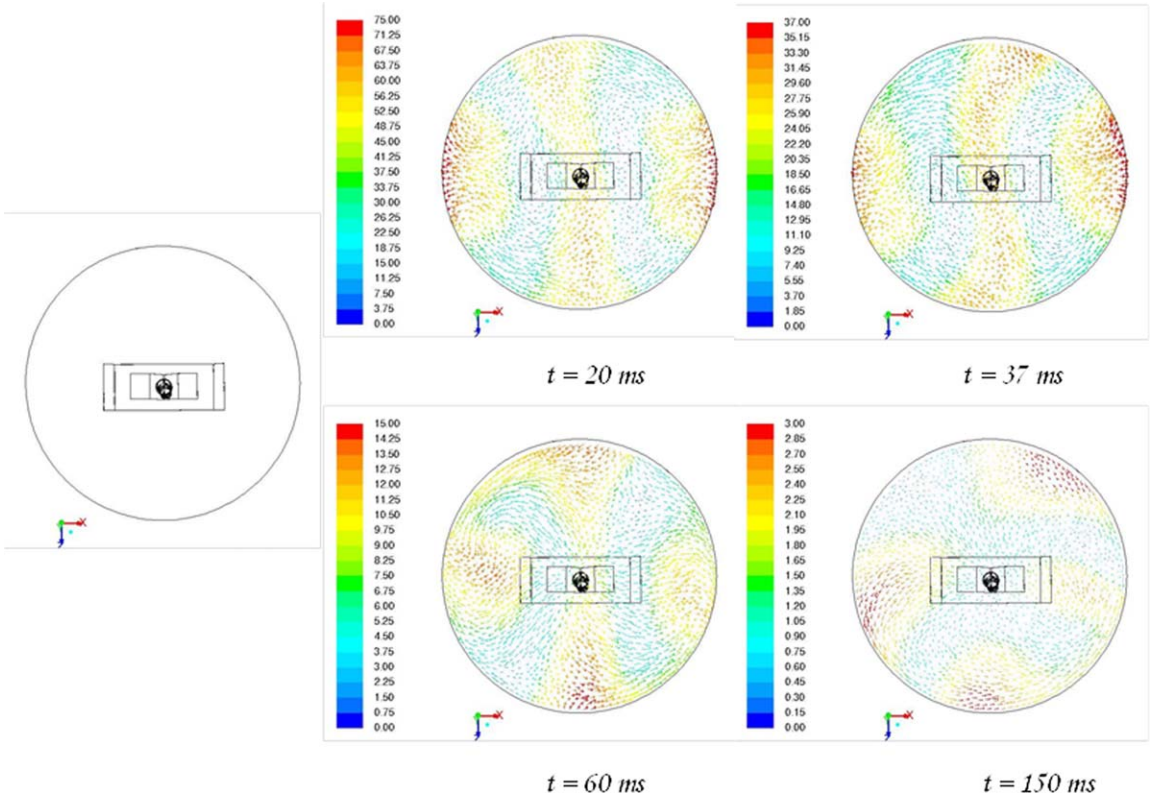

Figure 12. Time sequence of the maps of velocity vectors colored by the velocity magnitude (m/s): top view, dust-air mixture.

[Color figure can be viewed in the online issue, which is available at wileyonlinelibrary.com]

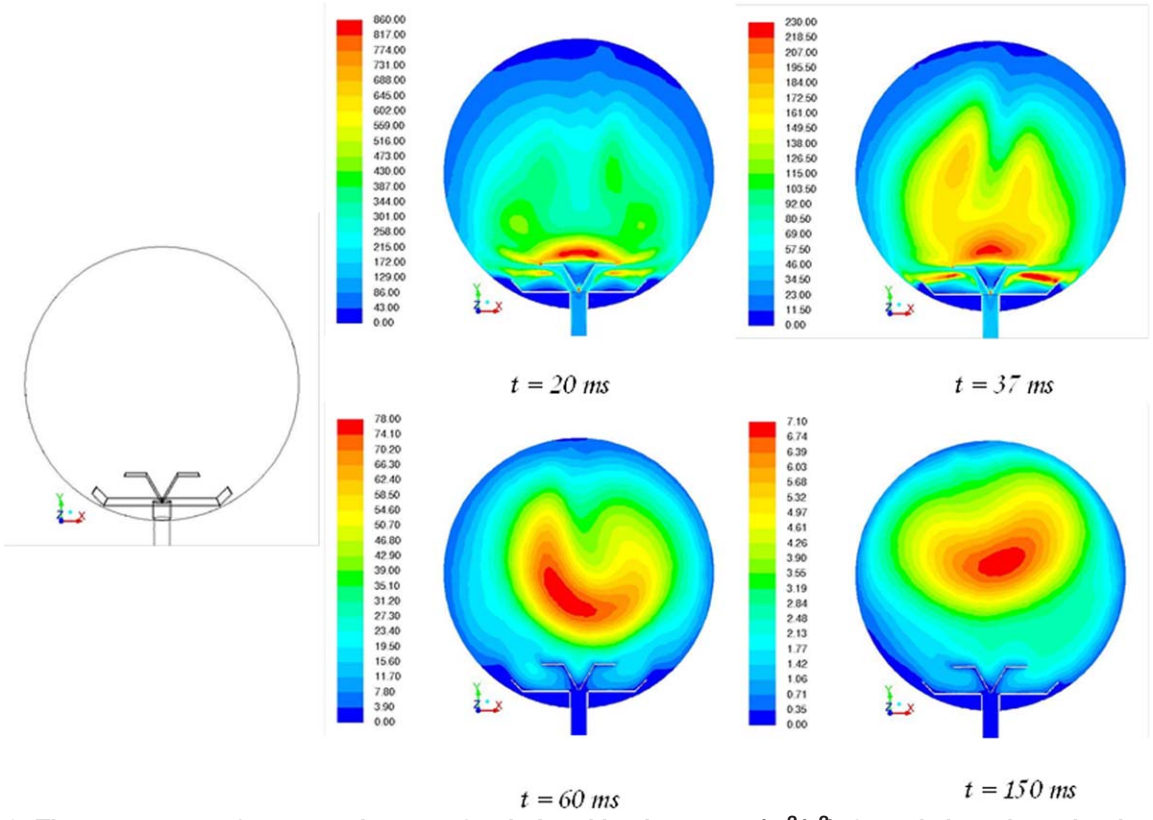

Figure 13. Time sequence of computed maps of turbulent kinetic energy (m^2/s^2): frontal view, dust-air mixture.

[Color figure can be viewed in the online issue, which is available at wileyonlinelibrary.com]

$$\tau_e = -T_L \log(n) \tag{8}$$

where n is a random number which varies in the range 0–1 and T_L depends on the turbulent kinetic energy and the dissipation rate

$$T_L \approx 0.15 \frac{k}{s} \tag{9}$$

Numerics

The governing fluid flow equations were discretized using a finite-volume formulation on the three-dimensional (3-D) nonuniform unstructured grid shown in the previous paragraph. The spatial discretization of the model equations used first-order schemes for convective terms and second-order schemes for diffusion terms. First-order time integration was used to discretize temporal derivatives with a time step of $1{\cdot}10^{-4}$ s.

Parallel calculations were performed by means of the segregated pressure-based solver of the code ANSYS Fluent (release 14). The semi-implicit method for pressure-linked equations (SIMPLE) was used to solve the pressure-velocity coupling. In order to achieve convergence, all residuals were set equal to $1{\cdot}10^{-6}$.

The discrete phase model was described by ordinary differential equations (on the contrary, the continuous flow was described by partial differential equations). Therefore, the DPM used its own numerical mechanisms and discretization schemes. For particle tracking, we used an automated scheme which provides a mechanism to switch in an automated fashion between numerically stable lower-order schemes and higher-order schemes, which are stable only in a limited range. In situations where the particle is far from hydrodynamic equilibrium, an accurate solution can be achieved very quickly with a higher-order scheme. When the particle reaches hydrodynamic equilibrium, the higher order schemes become inefficient and the mechanism switches to a stable lower order scheme. We choose the Euler integration as lower-order scheme and the semi-implicit trapezoidal integration as higher-order scheme. The particle tracking integration time step was taken equal to the fluid flow time step ($1{\cdot}10^{-4}$ s).

Simulation conditions

The fluid was air at constant atmospheric temperature. As initial conditions, we adopted the same conditions used in the standard tests: the container vessel (0.0006 m^3) was initially at pressure equal to 21 bar; the connecting tube and the sphere (0.02 m^3) were set to 0.4 bar.

Initially, the dust was not present in the container, but was artificially fed in 40 ms with a very low velocity ($1.\ 10^{-5}$ m/s). Dust properties are given in Table 3.

Results

Model validation

In Figure 6 (top), the pressure is plotted vs. time as computed in the sphere and in the container. From the pressure plots, the feeding phase during which air or dust-air mixture goes from the container to the sphere may be identified. This phase lasts 40 ms. Indeed, after 40 ms, the pressure in the sphere reaches 1 bar and the injection of air or dust-air comes to an end.

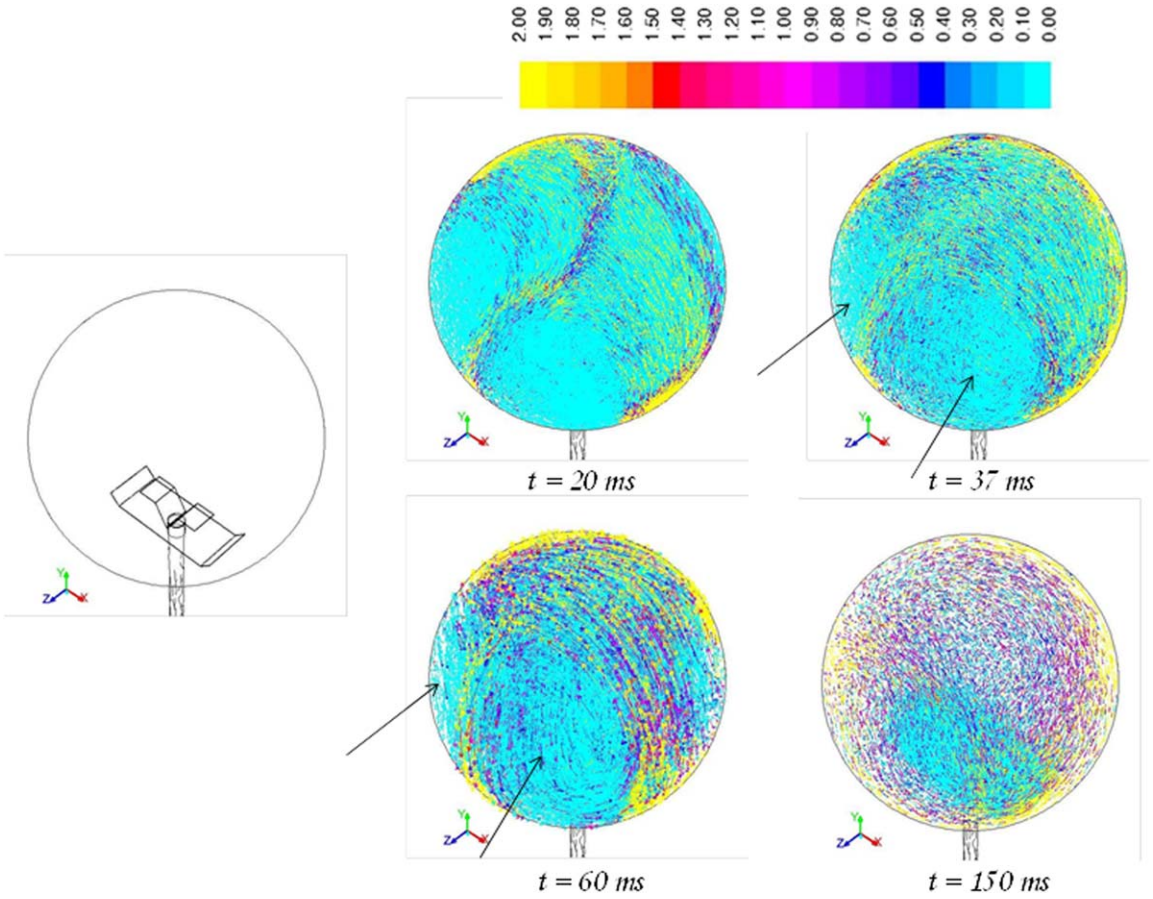

Figure 14. Time sequence of velocity vectors colored by γ as obtained in the whole sphere (oriented as in the empty image).

[Color figure can be viewed in the online issue, which is available at wileyonlinelibrary.com]

In Figure 6 (bottom), the time evolution of the dust concentration inside the sphere is shown. It is possible to verify that, when the pressure gradient between the sphere and the container goes to zero (40 ms), the dust concentration reaches its nominal value. It is also worth noting that the dust feeding is slow and after 25 ms the nominal concentration inside the sphere is equal to 50% of the nominal value. From this result, it appears that the ignition delay time cannot be lower than 40 ms. It is also worth underlying that the end time of the feeding phase may be significantly different when dust size and concentration are changed.

The model results in terms of temporal profile of pressure inside the sphere are compared to experimental data available in the literature[14,19]. The comparison shows a very good agreement.

In Figure 7, the corresponding temporal trend of the root mean square velocity is shown as computed in the same position (equatorial plane of the sphere) as in Dahoe et al.[20] We computed these trends in two different conditions: by feeding only air (-), and a dust-air mixture (-), with 10 μm dust size and 250 g/m^3 dust concentration. In the figure, the experimental data measured by Dahoe et al.[19] and de Heij[28] are also shown and compared to the model results. Both data of Dahoe et al.[19] relevant to vertical and horizontal velocity component fluctuations in experiments with only air are reported.

From Figure 7, it appears that there is a short period of turbulence build up followed by a much longer period of turbulence decay. The turbulence decay starts after few milliseconds from the opening of the valve, well before the end of the feeding phase. As also suggested by Dahoe et al.[19], this behavior can be attributed to the source term in the vorticity equation

$$\frac{\partial \omega}{\partial t} + v \cdot \nabla \omega = \omega \cdot \nabla v + v \nabla^2 \omega - \nabla \cdot \mathrm{v} + \frac{\nabla \rho \times \nabla \mathrm{p}}{\rho^2} \qquad (10)$$

where

$$\omega = \frac{1}{2} \nabla \times v \qquad (11)$$

When the pressure gradient decreases, the related source term $\left(\frac{\nabla\rho\times\nabla p}{\rho^2}\right)$ decreases as well. In these conditions, the turbulence generation reduces and the kinetic energy decreases.

Figure 7 shows that the model results obtained by feeding air (green curve) and dust-air (black curve) are very similar, thus suggesting that the presence of dust does not significantly affect the fluid flow.

de Heij[28] performed LDA measurements of the root mean square velocity at the center of the 20 L sphere, injecting different amounts of cornstarch dust (ranging from 125 up to 625 g/m^3). They concluded that the behavior of turbulent fluctuations is the same regardless of the presence of the dust. However, as also shown from their results, it turns out that a significant scatter of the data is found with the dust: the RMS velocity values may significantly differ at the same time when changing the dust concentration from 125 to 625 g/m^3.

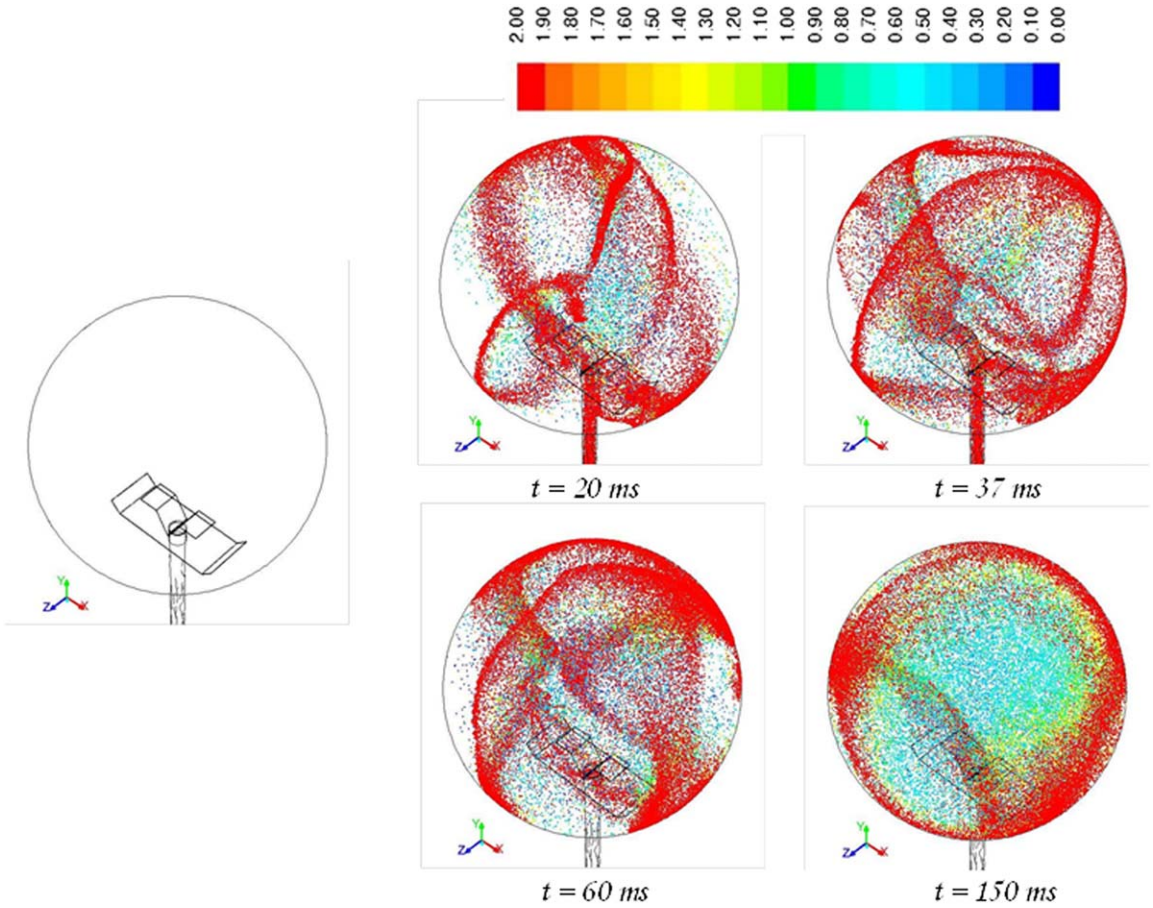

Figure 15. Time sequence of particle tracks colored by γ as obtained in the whole sphere (oriented as in the empty image).

[Color figure can be viewed in the online issue, which is available at wileyonlinelibrary.com]

We performed simulations by assuming only gas phase (air) and in the presence of dust (concentration equal to 250 g/m^3). The results are shown in Figure 7. It is found that the RMS curves are slightly different in the first 30 ms, while they overlap after 30 ms.

Future work should be devoted to the study of the combined role of dust concentration and dust diameter on the spatiotemporal distributions of velocity and turbulent kinetic energy. Indeed, the flow development is affected not only by the dust concentration, but also by the particle size.

Model Predictions

Velocity vector and turbulent kinetic energy maps: only air

In Figure 8, the time sequence of the maps of velocity vectors colored by the velocity magnitude are shown as computed over the frontal plane more clearly shown in the empty image of the figure (x-y plane) in the case of dust free air.

During the feeding phase ($t < 40$ ms), the gas velocity at the entrance is sonic. When the feeding phase has come to the end (i.e., $t = 60$ ms), the gas velocity significantly decreases, reaching its maximum at the lateral zones of the sphere (the main flow is here concentrated) and decaying in time. The figure also shows that two main vortices are formed at the center of the sphere. These vortices are well evident at 60 ms and appear to be almost dissipated at 150 ms.

In Figure 9, the time sequence of maps of the turbulent kinetic energy is shown as computed over the frontal (x-y) plane. The highest values of turbulent kinetic energy are attained during the feeding phase. After the feeding phase, the kinetic energy starts decaying.

During the feeding phase ($t < 40$ ms), strong spatial non uniformities are attained inside the sphere. Conversely, during the decaying phase ($t > 40$ ms), turbulence tends to become uniform at the center. In particular, at the typical ignition delay time ($t = 60$ ms), the turbulence distribution is almost uniform at the center of the sphere, where igniters are located.

Velocity vector and turbulent kinetic energy maps: dust-air mixture

In Figures 10–12, the time sequences of the maps of velocity vectors colored by the velocity magnitude are shown as computed over different planes of the sphere (more clearly shown in the empty images of each figure) in the case of dust-air mixture. Figure 10 shows the sequence over the frontal (x-y) plane (the same plane as in Figure 8).

It is worth noting that all figures return nonsymmetric fields, differently from the results obtained in the case of dust free air (Figures 8 and 9). This behavior has been previously found by Kartushinsky et al.[29] They developed a 3-D model of gas–solid particle flow in a horizontal pipe showing that the presence of particles in the flow has a significant effect on all flow variables. In particular, they pointed out that the distribution of all parameters becomes asymmetric, because of the gravitational effect on the particles and

particle sedimentation and physical effects related to the different densities of the two phases. The flow asymmetry cannot be accounted for in 2-D models.

Figure 11 shows the sequence over the lateral (y-z) plane. During the feeding phase ($t < 40$ ms), the maximum velocities correspond to the zone of the three holes. Once again, at the end of the feeding phase, the main flow is found at the lateral zones. Furthermore, at 60 ms, it is possible to see that two vortices are formed just behind the rebound nozzle. As already observed in Figure 8, these vortices almost disappear at 150 ms.

In Figure 12, the time sequence is shown as obtained over the top (x-z) plane that cuts the sphere across its middle section, and in Figure 13 the time sequence of maps of the turbulent kinetic energy is shown as computed over the frontal (x-y) plane. As already found for the velocity vector map (Figure 10), the presence of the dust gives rise to an asymmetric distribution of the kinetic energy. The asymmetric behavior has to be addressed to the particle sedimentation, as also suggested by Kartushinsky et al.[29]

Dust distribution and dispersion

The spatial-temporal distribution of dust concentration inside the sphere is represented through the ratio γ between the dust concentration and the nominal dust concentration ($C = 250$ g/m^3).

In Figure 14, the time sequence of the velocity vectors colored by γ is shown as obtained in the whole sphere oriented as in the empty image.

We can see that vortex structures form starting from 20 ms. Such structures become well defined at 60 ms (see the arrows). At this time, it appears that the highest dust concentrations are found close to the walls and, thus, in regions external to the vortices. Conversely, at the center of the vortices, the dust concentration is very low and much lower than the nominal value. This suggests that the dust is not entrained by the fluid and then the vortices are dead volume for the dust. When the feeding time is finished (i.e., $t \geq 60$ ms), the vortices damp out and the dust mainly accumulates at the wall.

Figure 15 shows the time sequence of the particle tracks colored by γ.

This figure further confirms that the highest dust concentrations are attained externally to the vortices, whereas the dust concentration is very low inside the vortices. In particular, at the typical ignition delay time ($t = 60$ ms), the dust is highly concentrated at the sphere walls, reaching concentrations much higher than the nominal value ($\gamma \approx 2$; C ≈ 500 g/m^3), while in the bulk of the sphere, the dust concentration is lower than the nominal value ($\gamma < 0.2$; C < 50 g/m^3). This result is qualitatively in agreement with the findings by Kalejaiye et al.[19] They measured the transmissions in different positions of the 20 L sphere. Lower values of transmission (and then higher values of concentration) were found in correspondence to the probes close to the vessel walls with respect to those closer to the sphere center. In addition, this result conforms with the observation that peak values of dp/dt_{max} in closed bomb experiments often occur at higher than stoichiometric concentrations.[8]

Conclusions

A 3-D CFD model was developed here to describe the turbulent flow field induced by dust feeding and dispersion within the 20 L bomb, and the associated effects on the distribution of dust concentration. This knowledge indeed plays a primary role in the determination of explosion parameters evaluated in the standard apparatus. The developed CFD model has been successfully validated against measurements of time histories of pressure and root mean square velocity available in the literature.

The time sequences of velocity vector and kinetic energy maps show that multiple turbulent vortex structures are established within the sphere. The presence of these vortices generates dead volumes for the dust which is pushed toward the walls of the sphere. The dust concentration is not uniform in the sphere, being higher close to the vessel walls and much lower than the nominal value inside the sphere. However, the turbulent kinetic energy is higher at the center of the sphere and, thus, close to the igniters.

Comparison between the results obtained in the cases of dust free air and dust-air mixture shows that, in the presence of dust, the fluid flow becomes asymmetric because of the entrainment effect of particle sedimentation.

Further studies are needed in order to evaluate the effect of dust size and size distribution, dust concentration and dust shape.

Literature Cited

1. Combustible Dust Hazard Study. Investigation Report-US. Chemical Safety and Hazard Investigation Board; 2006.
2. Salatino P, Di Benedetto A, Chirone R, Salzano E, Sanchirico R. Analysis of an explosion in a wool-processing plant. *Ind Eng Chem Res*. 2012;dx.doi.org/10.1021/ie2023614.
3. Dufaud O, Perrin L, Traoré M. Dust/vapour explosions: Hybrid behaviours? *J Loss Prev Process Ind*. 2008;21:481–484.
4. Dufaud O, Perrin L, Traoré M, Chazelet S, Thomas D. Explosions of vapour/dust hybrid mixtures: A particular class. *Powder Technol*. 2009;190:269–273.
5. Amyotte PR, Lindsay M, Domaratzki R, Marchand N, Di Benedetto A, Russo P. Prevention and mitigation of polyethylene and hydrocarbon/polyethylene explosions. Paper 7D. In: Proceedings of 43rd Annual Loss Prevention Symposium. AIChE 2009 Spring National Meeting, Tampa, FL, April 26–30; 2009:541–556.
6. Amyotte PR, Lindsay M, Domaratzki R, Marchand N, Di Benedetto A, Russo P. Prevention and mitigation of dust and hybrid mixture explosions. *Process Saf Prog*. 2010; 29:17–21.
7. Garcia-Agreda A, Di Benedetto A, Russo P, Salzano E, Sanchirico R. Dust/gas mixtures explosion regimes. *Powder Technol*. 2005;205:81–86.
8. Eckhoff RK. Explosions in the Process Industries. 3rd ed. Gulf Professional Publishing; 2003.
9. Di Benedetto A, Russo P. Thermo-kinetic modelling of dust explosions. *J Loss Prev Process Ind*. 2007;20:303–309.
10. Di Benedetto A, Russo P, Amyotte PR, Marchand N. Modelling the effect of particle size on dust explosions. *Chem Eng Sci*. 2010;65:771–779.
11. Continillo G. A two-zone model and a distributed-parameters model of dust explosions in closed vessels. *Arch Combust*. 1989;9:79–94.
12. Eckhoff RK. Differences and similarities of gas and dust explosions: A critical evaluation of the European 'ATEX' directives in relation to dusts. *J Loss Prev Process Ind*. 2006;19:553–560.
13. Cashdollar KL. Coal dust explosibility. *Journal of Loss Prevention in the Process Industries*. 1996; 9:65–67.
14. Di Benedetto A, Garcia-Agreda A, Russo P, Sanchirico R. Combined effect of ignition energy and initial turbulence on the explosion behavior of lean gas/dust-air mixtures. *Ind Eng Chem Res*. 2012.dx.doi.org/10.1021/ie201664a.
15. Bartknecht W. Dust Explosions: Course, Prevention, Protection. Berlin: Springer-Verlag; 1989.
16. Siwek R. Reliable determination of the safety characteristics in 20-l apparatus. In: Proceedings of the Flammable Dust Explosion Conference; St. Louis: MO; 1988:529–573.

17. Pu YK, Jarosinski J, Johnson VG, Kauffman CW. Turbulence effects on dust explosions in the 20-L spherical vessel. In: Proceedings of 23rd International Symposium on Combustion. Pittsburgh, PA: The Combustion Institute; 1990:843–849.
18. van der Wel PGJ, van Veen JPW, Lemkowitz SM, Scarlett B, van Wingerden, CJM. An interpretation of dust explosion phenomena on the basis of time scales. *Powder Technol*. 1992; 71:207–215.
19. Dahoe AE, Cant RS, Scarlett B. On the decay of turbulence in the 20-liter explosion sphere. *Flow Turb Combust*. 2001;67:159–184.
20. Hauert F, Vogl A, Radandt S. Measurement of turbulence and dust concentration in silos and vessels. In Proceedings of the 6th International Colloquium on Dust Explosions, Shenyang, PRC. 1994.
21. Zhen G, Leuckel W. Determination of dust-dispersion induced turbulence and its influence on dust explosions. *Combust Sci Technol*. 1996;113:629–639.
22. Kalejaiye O, Amyotte PR, Pegg MJ, Cashdollar KL. Effectiveness of dust dispersion in the 20-L Siwek chamber. *J Loss Prev Process Ind*. 2010;23:46–59.
23. Code ANSYS FLUENT, www.ansys.com.
24. Launder BE, Spalding DB. Lectures in mathematical models of turbulence. London, UK: Academic Press; 1972.
25. Elghobashi S. On predicting particle-laden turbulent flows. *Appl Sci Res*. 1994;52:309–329.
26. Vreman B, Geurts BJ, Deen NG, Kuipers JAM, Kuerten JGM. Two- and four-way coupled euler-lagrangian large-eddy simulation of turbulent particle-laden channel flow. *Flow Turb Combust*. 2009;82:47–71.
27. Laín S, Sommerfeld M, Quintero B. Numerical simulation of secondary flow in a pneumatic conveying of solid particle in a horizontal circular pipe. *Brazilian J Chem Eng*. 2009;26:583–594.
28. de Heij WBC. On the Application of Laser Doppler Anemometry to the Transient low inside the standard 20-litre explosion sphere [Master's Thesis]. Delft, The Netherlands: Delft University of Technology; 1998.
29. Kartushinsky AI, Michaelides EE, Rudi YA, Tisler SV, Shcheglov IN. Numerical simulation of three-dimensional gas–solid particle flow in a horizontal pipe. *AIChE J*. 2011;57:2977–2988.

Manuscript received May 23, 2012, and revision received Dec. 14, 2012.